Aerodynamic Shape Optimization by Space Mapping

Leifur Leifsson, Slawomir Koziel, Eirikur Jonsson, and Stanislav Ogurtsov

Abstract Space mapping (SM) has been successfully applied in various fields of engineering and science. However, despite its potential, SM has only recently been applied in aerospace engineering. This chapter describes recent advances in aerodynamic design and optimization using SM. In particular, a detailed formulation of the optimization methodology is provided, as well as several applications involving the design of transonic airfoils and wings.

Keywords Aerodynamic shape optimization · Space mapping · CFD

1 Introduction

Aerodynamic shape optimization (ASO) is a field of engineering that couples optimization methods and fluid flow analysis to design streamlined surfaces. ASO is important in the design of a number of engineering systems and devices, such as aircraft [1], turbomachinery [2], and automotive [3] and marine vehicles [4]. Nowadays, high-fidelity computational fluid dynamic (CFD) simulations are widely used in the design process. Although CFD analyses are accurate and reliable, they can be computationally expensive. Therefore, efficient and robust design algorithms are essential for rapid optimization.

Computationally efficient ASO can be performed using surrogate-based optimization (SBO) techniques [5–7]. In SBO, direct optimization of the high-fidelity

L. Leifsson (✉) · S. Koziel · E. Jonsson · S. Ogurtsov
Engineering Optimization & Modeling Center, School of Science and Engineering, Reykjavik University, Menntavegur 1, 101 Reykjavik, Iceland
e-mail: leifurth@ru.is

S. Koziel
e-mail: koziel@ru.is

E. Jonsson
e-mail: eirikurjon07@ru.is

S. Ogurtsov
e-mail: stanislav@ru.is

CFD model is replaced by an iterative correction-prediction process where a surrogate model (a computationally cheap representation of the high-fidelity one) is constructed and subsequently exploited to obtain an approximate location of the high-fidelity model optimal design.

A surrogate model can be constructed by approximating sampled high-fidelity model data using, e.g., polynomial approximation [5], radial basis functions [6, 8], kriging [7, 9–11], neural networks [12, 13], or support vector regression [14] (response surface approximation surrogates) or by correcting/enhancing a physics-based low-fidelity model (physical surrogates) [7, 15]. Approximation surrogates usually require a large number of high-fidelity model evaluations to ensure decent accuracy, and the number of samples typically grows exponentially with the number of design variables. On the other hand, approximation surrogates can be a basis of efficient global optimization techniques [6]. Various techniques of updating the training data set (the so-called infill criteria [6]) have been developed that aim at obtaining global modeling accuracy, locating a globally optimal design, or achieving a trade-off between the two, particularly in the context of kriging interpolation [6].

Physics-based surrogate models are not as versatile as approximation ones, because they rely on the underlying low-fidelity model (a simplified description of the system). Low-fidelity models can be obtained by neglecting certain second-order effects, using simplified equations, or—probably the most versatile approach—by exploiting the same CFD solver as used to evaluate the high-fidelity model but with a coarser mesh and/or relaxed convergence criteria [16]. It seems that physical surrogates have the potential to offer better efficiency in terms of reducing the computational cost of the design process. The reason is that the knowledge about the system of interest embedded into the low-fidelity model allows us to construct a quality surrogate model using a limited amount of high-fidelity model data. For many practical algorithms, only a single high-fidelity model evaluation is sufficient [7, 17]. For the same reason, physical surrogates have much better generalization capability than the approximation models [17].

Several SBO algorithms exploiting physical surrogates have been proposed in the literature, including approximation and model management optimization (AMMO) [18], space mapping (SM) [17, 19], manifold mapping (MM) [20], and, recently, shape-preserving response prediction (SPRP) [21]. All of these methods differ in the specific method of using the low-fidelity model to create the surrogate. Space mapping is probably the most popular approach of this kind. It was originally developed for simulation-driven design in microwave engineering [17]; however, it is currently becoming more and more popular in other areas of engineering and science (see [17, 19]). Despite its potential, space mapping has only recently been applied in ASO [22–24].

In this chapter, we describe a computationally efficient ASO methodology which employs physics-based surrogate models created by space mapping [23, 24]. Section 2 briefly describes aerodynamic shape design and the optimization problem. The optimization methodology is described in detail in Sect. 3. Applications of the method to transonic airfoil and wing design are given in Sects. 4, 5. Section 6 summarizes the chapter.
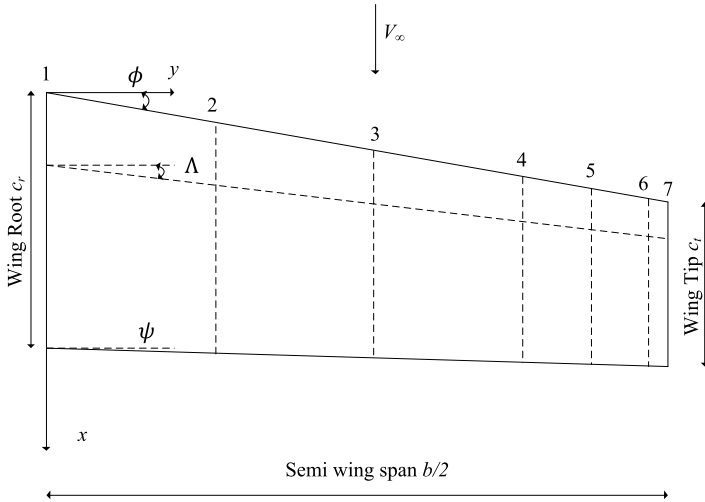
Fig. 1 Planform view of a trapezoidal wing (or a turbine blade) of a semi-span $b/2$ and quarter chord sweep angle Λ. Span stations are marked 1 through 7 and the free-stream velocity is V_∞. Leading edge and trailing edge angles ϕ and ψ are also shown. Other design parameters are not shown

2 Aerodynamic Shape Design

The fundamentals of aerodynamic shape design are briefly addressed in this section. In particular, the geometry description, figures of merit, and the optimization problem are defined.

2.1 Geometry

A three-dimensional streamlined aerodynamic surface is depicted in Fig. 1, which could, for example, represent a simple aircraft wing or a turbine blade. Design parameters controlling the planform shape include the semi-span ($b/2$), the quarter chord wing sweep angle (Λ), the thickness-to-chord ratio (t/c) at each span station, the wing taper ratio (λ), and the twist distribution (γ).

At each span station (numbered 1 through 7) of the surface, the cross section is defined by an airfoil profile such as the one in Fig. 2. The number of span stations can be larger or fewer than shown here and depends on the particular design scenario. A straight line wrap is often assumed between the span stations. The airfoil shapes are characterized by the chord length (c), thickness distribution (t), and camber distribution. Designable parameters controlling the overall shape depend on the parameterization technique employed by the designer. Examples of such techniques include the National Advisory Committee for Aeronautics (NACA) four-digit airfoil shapes [25], the Hicks and Henne bump functions [26], and the Bezier-PARSEC method [27], each with different types and numbers of control parameters.
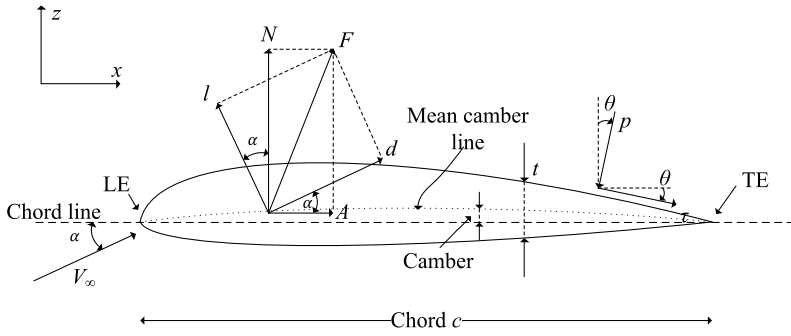
Fig. 2 Airfoil wing cross section (*solid line*) of thickness t and chord length c. V_∞ is the free-stream velocity and is at an angle of attack α relative to the x-axis. F is the resulting aerodynamic force, where l is the lift force, perpendicular to V_∞, and d is the drag force, parallel to V_∞. p is the pressure acting normal to a surface element ds. τ is the viscous wall shear stress acting parallel to the surface element. θ is the angle that p and τ make relative to the z-axis and x-axis, respectively, where a positive angle is clockwise

2.2 Figures of Merit

In general, a streamlined aerodynamic surface is designed to provide a certain lift at a minimum drag. In ASO, the typical figures of merit are the lift and drag coefficients. The lift coefficient (for a three-dimensional surface) is defined as

$$C_L = \frac{L}{q_\infty S},\tag{1}$$

and the drag coefficient as

$$C_D = \frac{D}{q_\infty S},\tag{2}$$

where S is a reference area (usually chosen as the planform area), L and D are the magnitude of the total lift and drag forces, respectively, and the dynamic pressure q_∞ is defined as

$$q_\infty = \frac{1}{2}\rho_\infty V_\infty,\tag{3}$$

where ρ_∞ is the free-stream density and V_∞ is the magnitude of the free-stream velocity.

The forces acting on the surface are calculated from the results of a numerical simulation of the flow past it. In particular, the lift and drag coefficients can be calculated as

$$C_L = -C_A \sin\alpha + C_N \cos\alpha,\tag{4}$$

and

$$C_D = C_A \cos\alpha + C_N \sin\alpha,\tag{5}$$

Table 1 Various problem formulations for aerodynamic shape optimization. Typically, constraints on the minimum allowable cross-sectional area are also included, i.e., $c_2(\mathbf{x}) = A_{\min}(\mathbf{x}) - A(\mathbf{x}) \leq 0$, where $A_{\min}(\mathbf{x})$ is the minimum cross-sectional area at a given span station. $C_{p.t}$ is a target pressure distribution

Case	$f(\mathbf{x})$	$c_1(\mathbf{x})$
Lift maximization	$-C_L(\mathbf{x})$	$C_D(\mathbf{x}) - C_{D.\min} \leq 0$
Drag minimization	$C_D(\mathbf{x})$	$C_{L.\max} - C_L(\mathbf{x}) \leq 0$
L/D maximization	$-C_L(\mathbf{x})/C_D(\mathbf{x})$	$C_{L.\max} - C_L(\mathbf{x}) \leq 0$
Inverse design	$1/2 \int (C_p(\mathbf{x}) - C_{p.t})^2 \, ds$	

respectively. Here, the nondimensional force coefficients parallel to the x- and z-axes, C_A and C_N, respectively, are calculated by integrating the pressure distribution (C_p) and the skin friction distribution (C_f) over the surface as

$$C_A = \oint (C_p \sin\theta + C_f \cos\theta) \, ds, \tag{6}$$

and

$$C_N = \oint (-C_p \cos\theta + C_f \sin\theta) \, ds, \tag{7}$$

where ds is the length of the surface panel element and θ is the angle of the panel relative to the x-axis (see definition in Fig. 2).

2.3 Optimization Problem

Generally, aerodynamic shape optimization can be formulated as a nonlinear minimization problem; i.e., for a given operating condition, solve

$$
\begin{aligned}
\min_{\mathbf{x}} \quad & f(\mathbf{x}) \\
\text{s.t.} \quad & c_j(\mathbf{x}) \leq 0 \\
& \mathbf{l} \leq \mathbf{x} \leq \mathbf{u},
\end{aligned}
\tag{8}
$$

where $f(\mathbf{x})$ is the objective function, $\mathbf{x}$ is the design variable vector, $c_j(\mathbf{x})$ is a design constraint ($j = 1, \ldots, N$ and N is the number of constraints), and $\mathbf{l}$ and $\mathbf{u}$ are the lower and upper bounds for the design variables, respectively. The design variables and the detailed formulation are problem-specific, but typical formulations are shown in Table 1. Other constraints such as mathematical models describing the structural weight of the wing are often included in optimization [28].

3 Space Mapping for Aerodynamic Design

In this section, we describe a space mapping (SM) optimization methodology for aerodynamic shape design. First, the aerodynamic optimization problem described in the previous section is formulated for the SM approach. Then, we briefly recall some SM basics, and define the surrogate model construction. Finally, the SM algorithm is described.

3.1 Problem Formulation

A simulation-driven design can be formulated as a nonlinear minimization problem as noted before. Refining (8), we define

$$\mathbf{x}^* = \arg\min_{\mathbf{x}} H\big(f(\mathbf{x})\big), \tag{9}$$

where $\mathbf{x}$ is a vector of design parameters, f the high-fidelity model to be minimized at $\mathbf{x}$, and H is the objective function. $\mathbf{x}^*$ is the optimum design vector. The high-fidelity model will represent aerodynamic forces, the lift and drag coefficients, as well as other scalar responses such as the cross-sectional area A of the wing at the location of interest. The area response can be of a vector form $\mathbf{A}$ if one requires multiple area cross-sectional constraints at various locations on the wing, e.g., the wing root and the wing tip. The response will have the form

$$f(\mathbf{x}) = \begin{bmatrix} C_{L.f}(\mathbf{x}) & C_{D.f}(\mathbf{x}) & A_f(\mathbf{x}) \end{bmatrix}^T, \tag{10}$$

where $C_{L,f}$ and $C_{D,f}$ are the lift and drag coefficients, respectively, generated by the high-fidelity model. We are interested in maximizing lift or minimizing drag, so the objective function will take the form

$$H\big(f(\mathbf{x})\big) = -C_L, \tag{11}$$

or

$$H\big(f(\mathbf{x})\big) = C_D, \tag{12}$$

respectively, with the design constraints denoted as

$$C\big(f(\mathbf{x})\big) = \begin{bmatrix} c_1(f(\mathbf{x})) & \dots & c_k(f(\mathbf{x})) \end{bmatrix}^T. \tag{13}$$

Maximizing lift will yield two nonlinear design constraints for drag and area,

$$c_1\big(f(\mathbf{x})\big) = C_{D,f}(\mathbf{x}) - C_{D,\max} \leq 0, \tag{14}$$

$$c_2\big(f(\mathbf{x})\big) = -A_f(\mathbf{x}) + A_{\min} \leq 0. \tag{15}$$

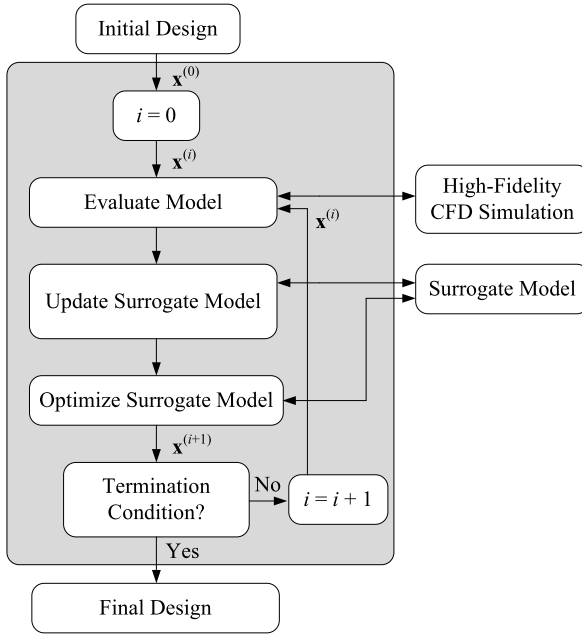**Fig. 3** A flow diagram of a generic SBO algorithm

Similarly, minimizing drag we have two nonlinear design constraints for lift and area,

$$c_1\big(f(\mathbf{x})\big) = -C_{L,f}(\mathbf{x}) + C_{L,\min} \leq 0, \tag{16}$$

$$c_2\big(f(\mathbf{x})\big) = -A_f(\mathbf{x}) + A_{\min} \leq 0. \tag{17}$$

3.2 Space Mapping Basics

Space mapping (SM) [17, 19] is a surrogate-based optimization (SBO) technique where the computational burden is shifted from an expensive high-fidelity model (or fine model), denoted by f, to a cheaper model, the surrogate, denoted by s, where the surrogate is iteratively optimized and updated. The flow of a typical SBO algorithm is shown in Fig. 3.

Starting from a initial design $\mathbf{x}^{(0)}$, the genetic SM algorithm produces a sequence $\mathbf{x}^{(i)}$, $i = 0, 1, \dots$ of an approximate solution to (9) as

$$\mathbf{x}^{(i+1)} = \arg\min_{\mathbf{x}} H\big(s^{(i)}(\mathbf{x})\big), \tag{18}$$

where

$$s^{(i)}(\mathbf{x}) = \big[C_{L.s}^{(i)}(\mathbf{x}) \quad C_{D.s}^{(i)}(\mathbf{x}) \quad A_s(\mathbf{x})^{(i)}\big]^T \tag{19}$$

is the surrogate model at iteration i. As previously described, the accurate high-fidelity CFD model f is accurate but computationally expensive. Using SM, the surrogate s is a composition of the low-fidelity CFD model c and a simple linear transformation to correct the low-fidelity model response [17]. The corrected response is denoted as $s(\mathbf{x}, \mathbf{p})$, where $\mathbf{p}$ represents a set of model parameters and at iteration i the surrogate is

$$s^{(i)}(\mathbf{x}) = s(\mathbf{x}, \mathbf{p}). \tag{20}$$

The SM parameters $\mathbf{p}$ are determined through a parameter extraction (PE) process [17]. In general, this process is a nonlinear optimization problem, where the objective is to minimize the misalignment of the surrogate response at some or all previous iterations of the high-fidelity model data points [17]. The PE optimization problem can be defined as

$$\mathbf{p}^{(i)} = \arg\min_{\mathbf{p}} \sum_{k=0}^{i} w_{i,k} \left\| f(\mathbf{x}^{(k)}) - s(\mathbf{x}^{(k)}, \mathbf{p}) \right\|^2, \tag{21}$$

where $w_{i,k}$ are weight factors that control how much impact previous iterations affect the SM parameters. Popular choices are

$$w_{i,k} = 1 \quad \forall i, k, \tag{22}$$

and

$$w_{i,k} = \begin{cases} 1 & k = i, \\ 0 & \text{otherwise.} \end{cases} \tag{23}$$

In the latter case, the parameters only depend on the most recent SM iteration.

Examples of SM surrogate models include input SM, where $s(\mathbf{x}, \mathbf{p}) = s(\mathbf{x}, \mathbf{q}) = c(\mathbf{x} + \mathbf{q})$ (parameter shift) or $s(\mathbf{x}, \mathbf{p}) = s(\mathbf{x}, \mathbf{B}, \mathbf{q}) = c(\mathbf{B}\mathbf{x} + \mathbf{q})$ (parameter shift and scaling), output SM, with $s(\mathbf{x}, \mathbf{p}) = s(\mathbf{x}, \mathbf{A}) = \mathbf{A}c(\mathbf{x})$ (multiplicative response correction) or $s(\mathbf{x}, \mathbf{p}) = s(\mathbf{x}, \mathbf{d}) = c(\mathbf{x}) + \mathbf{d}$ (additive response correction), and a few others such as implicit SM [29] and frequency SM [30].

3.3 Surrogate Model Construction

The SM surrogate model s is a composition of a low-fidelity model c and corrections or linear transformations, where the model parameters p are extracted using one of the PE processes described above. PE and surrogate optimization create a certain overhead on the whole process, and this overhead can be a significant part of the overall computational cost. This is mainly due to the fact that the physics-based low-fidelity models are, in general, relatively expensive to evaluate compared to the functional-based ones. Despite this, SM may be beneficial [31].

This problem can be alleviated by exploiting the output SM with both multiplicative and additive response corrections where the surrogate model parameters are extracted analytically. The surrogate model is then written as

$$s^{(i)}(\mathbf{x}) = \mathbf{A}^{(i)} \circ c(\mathbf{x}) + \mathbf{D}^{(i)} + \mathbf{q}^{(i)} \tag{24}$$

$$= \left[a_L^{(i)} C_{L.c}(\mathbf{x}) + d_L^{(i)} + q_L^{(i)} \quad a_D^{(i)} C_{D.c}(\mathbf{x}) + d_D^{(i)} + q_D^{(i)} \quad A_c(\mathbf{x}) \right]^T, \tag{25}$$

where $\circ$ is a component-wise multiplication. No mapping is needed for the area $A_c(\mathbf{x})$, where $A_c(\mathbf{x}) = A_f(\mathbf{x}) \; \forall \mathbf{x}$ since the low- and high-fidelity models represent the same geometry. Parameters $\mathbf{A}^{(i)}$ and $\mathbf{D}^{(i)}$ are obtained using

$$\left[\mathbf{A}^{(i)}, \mathbf{D}^{(i)} \right] = \arg\min_{\mathbf{A}, \mathbf{D}} \sum_{k=0}^{i} \left\| f\left(\mathbf{x}^{(k)}\right) - \mathbf{A} \circ c\left(\mathbf{x}^{(k)}\right) + \mathbf{D} \right\|^2, \tag{26}$$

where $w_{i,k} = 1$; i.e., all previous iteration points are used to globally improve the response of the low-fidelity model. The additive term $q^{(i)}$ is defined so as to ensure this perfect match between the surrogate and the high-fidelity model at design $\mathbf{x}^{(i)}$, namely $f(\mathbf{x}^{(i)}) = s(\mathbf{x}^{(i)})$ or a zero-order consistency [18]. We can write the additive term as

$$q^{(i)} = f\left(\mathbf{x}^{(i)}\right) - \left[\mathbf{A}^{(i)} \circ c\left(\mathbf{x}^{(i)}\right) + \mathbf{D}^{(i)} \right]. \tag{27}$$

Since an analytical solution exists for $\mathbf{A}^{(i)}, \mathbf{D}^{(i)}$, and $\mathbf{q}^{(i)}$, there is no need for nonlinear optimization solving (21) to obtain parameters. We can obtain $\mathbf{A}^{(i)}$ and $\mathbf{D}^{(i)}$ as

$$\begin{bmatrix} a_L^{(i)} \\ d_L^{(i)} \end{bmatrix} = \left(\mathbf{C}_L^T \mathbf{C}_L \right)^{-1} \mathbf{C}_L^T \mathbf{F}_L, \tag{28}$$

$$\begin{bmatrix} a_D^{(i)} \\ d_D^{(i)} \end{bmatrix} = \left(\mathbf{C}_D^T \mathbf{C}_D \right)^{-1} \mathbf{C}_D^T \mathbf{F}_D, \tag{29}$$

where

$$\mathbf{C}_L = \begin{bmatrix} C_{L.c}(\mathbf{x}^{(0)}) & C_{L.c}(\mathbf{x}^{(1)}) & \dots & C_{L.c}(\mathbf{x}^{(i)}) \\ 1 & 1 & \dots & 1 \end{bmatrix}^T, \tag{30}$$

$$\mathbf{F}_L = \begin{bmatrix} C_{L.f}(\mathbf{x}^{(0)}) & C_{L.f}(\mathbf{x}^{(1)}) & \dots & C_{L.f}(\mathbf{x}^{(i)}) \\ 1 & 1 & \dots & 1 \end{bmatrix}^T, \tag{31}$$

$$\mathbf{C}_D = \begin{bmatrix} C_{D.c}(\mathbf{x}^{(0)}) & C_{D.c}(\mathbf{x}^{(1)}) & \dots & C_{D.c}(\mathbf{x}^{(i)}) \\ 1 & 1 & \dots & 1 \end{bmatrix}^T, \tag{32}$$

$$\mathbf{F}_D = \begin{bmatrix} C_{D.f}(\mathbf{x}^{(0)}) & C_{D.f}(\mathbf{x}^{(1)}) & \dots & C_{D.f}(\mathbf{x}^{(i)}) \\ 1 & 1 & \dots & 1 \end{bmatrix}^T, \tag{33}$$

and these are the least-square optimal solutions to the linear regression problems

$$\mathbf{C}_L a_L^{(i)} + d_L^{(i)} = \mathbf{F}_L, \tag{34}$$

$$\mathbf{C}_D a_D^{(i)} + d_D^{(i)} = \mathbf{F}_D. \tag{35}$$

Note that $\mathbf{C}_L^T \mathbf{C}_L$ and $\mathbf{C}_L^T \mathbf{C}_L$ are nonsingular for $i > 1$ and $\mathbf{x}^{(k)} \neq \mathbf{x}^{(i)}$ for $k \neq i$. For $i = 1$ only the multiplicative SM correction with $\mathbf{A}^{(i)}$ is used.

3.4 Algorithm

The SM optimization algorithm, exploiting the trust region convergence safeguard [6], is as follows:

1. Set $i = 0$; Select λ, the trust region radius; Evaluate the high-fidelity model at the initial solution, $f(\mathbf{x}^{(0)})$;
2. Using data from the low-fidelity model c, and f at $\mathbf{x}^{(k)}, k = 0, 1, \ldots, i$, set up the SM surrogate $s^{(i)}$; Perform PE;
3. Optimize $s^{(i)}$ to obtain $\mathbf{x}^{(i+1)}$;
4. Evaluate $f(\mathbf{x}^{(i+1)})$;
5. If $H(f(\mathbf{x}^{(i+1)})) < H(f(\mathbf{x}^{(i)}))$, accept $\mathbf{x}^{(i+1)}$; Otherwise set $\mathbf{x}^{(i+1)} = \mathbf{x}^{(i)}$;
6. Update λ;
7. Set $i = i + 1$;
8. If the termination condition is not satisfied, go to 2, else proceed;
9. End; Return $\mathbf{x}^{(i)}$ as the optimum solution.

Note that the trust region parameter λ is updated after each iteration.

4 Airfoil Design

The use of the SM algorithm is demonstrated here for the design optimization of airfoil shapes at transonic flow conditions. A steady inviscid Euler CFD model is used with a structured grid for both the high- and low-fidelity models, but with different grid resolution and convergence criteria (variable-resolution models). The algorithm is applied to both lift maximization and drag minimization.

4.1 High-Fidelity Model

The flow is assumed to be steady, inviscid, and adiabatic with no body forces. The compressible Euler equations are taken to be the governing fluid flow equations (see, e.g., [32]). The solution domain boundaries are placed at 25 chord lengths in front of the airfoil, 50 chord lengths behind it, and 25 chord lengths above and below
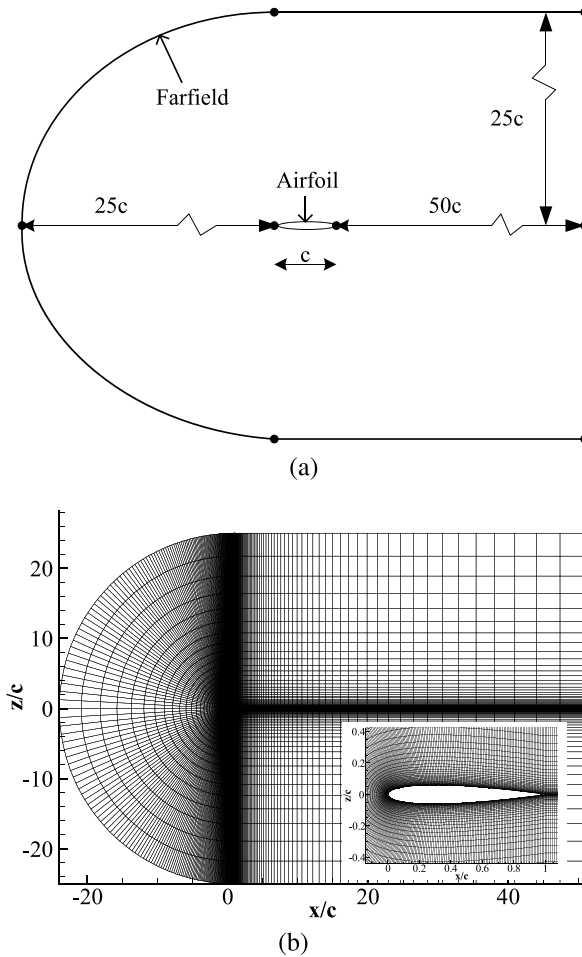
(a)

(b)

Fig. 4 Particulars of the two-dimensional solution domain and the grid: (**a**) a sketch of the computational domain for the flow past an airfoil with a chord length c, (**b**) example grid for the NACA 0012 airfoil

it (see Fig. 4). The computational meshes are of structured curvilinear body-fitted C-topology with elements clustering around the airfoil and growing in size with distance from the airfoil surface. The computer code ICEM CFD [33] is used for the mesh generation. The free-stream Mach number, static pressure, and angle of attack are prescribed at the far-field boundary.

   Numerical fluid flow simulations are performed using the computer code FLU-ENT [34]. The flow solver is of an implicit density-based formulation, and the inviscid fluxes are calculated by an upwind-biased second-order spatially accurate Roe flux scheme. Asymptotic convergence to a steady state solution is obtained for each case. The iterative convergence of each solution is examined by monitoring the
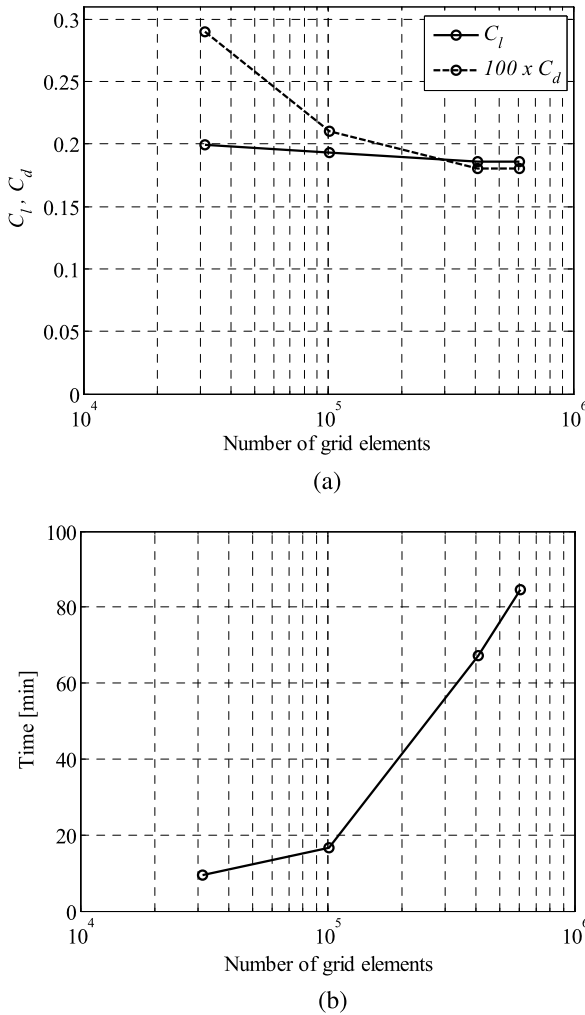
(a)

(b)

Fig. 5 Grid convergence study using the NACA 0012 airfoil at Mach number $M_\infty = 0.75$ and angle of attack $\alpha = 1$ deg: (**a**) lift and drag coefficients versus the number of grid elements, and (**b**) the simulation time versus the number of grid elements

overall residual, which is the sum (over all the cells in the computational domain) of the L^2 norm of all the governing equations solved in each cell. In addition to this, the lift and drag forces (defined in Sect. 2) are monitored for convergence. The solution convergence criterion for the high-fidelity model is the one that occurs first of the following: a maximum residual of 10^{-6}, or a maximum number of iterations of 1,000.

A grid convergence study was performed using the NACA 0012 airfoil at Mach number $M_\infty = 0.75$ and angle of attack $\alpha = 1$ deg. The study, shown in Fig. 5a,

revealed that 407,676 mesh cells are needed for mesh convergence; thus, that particular mesh was used for the high-fidelity model. The overall simulation time for the case considered is around 67 min (Fig. 5b). The flow solver reached a converged solution after 352 iterations. The other meshes required around 350 to 500 iterations to converge, except the coarsest mesh, which terminated after 1,000 iterations, with an overall simulation time of around 9.5 min.

4.2 Low-Fidelity Model

The low-fidelity CFD model is constructed in the same way as the high-fidelity model, but with a coarser computational mesh and relaxed convergence criteria. For the low-fidelity model, we use the coarse mesh in the grid study presented in Fig. 5a, with 31,356 mesh cells. The flow solution history for the low-fidelity model, shown in Fig. 6a, indicates that the lift and drag coefficients are nearly converged after 80 to 100 iterations. The maximum number of iterations is set to 100 for the low-fidelity model. This reduced the overall simulation time to 1.5 min. A comparison of the pressure distributions, shown in Fig. 6b, indicates that the low-fidelity model, despite being based on a much coarser mesh and reduced flow solver iterations, captures the main features of the high-fidelity model pressure distribution quite well. The biggest discrepancy in the distributions is around the shock on the upper surface, leading to an overestimation of both lift and drag (Fig. 5a).

The ratio of simulation times of the high- and low-fidelity model in this particular case study is 43.8. In many cases, the solver does not fully converge with respect to the residuals and goes on up to 1,000 iterations. Then, the overall evaluation time of the high-fidelity model goes up to 170 min. In those cases, the ratio of simulation times of the high- and low-fidelity models is around 110. For simplicity, we will use a fixed value of 80 when estimating the equivalent number of function calls, i.e., when the number of low-fidelity function calls is added to the number of high-fidelity function calls.

4.3 Surrogate Model

The surrogate model is constructed using (24). The responses for a few randomly selected airfoil geometries using the low-fidelity model $c(\mathbf{x})$ (selected in the previous section) and the high-fidelity model $f(\mathbf{x})$ are shown in Fig. 7, as well as the globally corrected surrogates $A \circ c(\mathbf{x}) + D$, calculated using (26). Note that output SM is capable of substantially reducing the misalignment between the surrogate and high-fidelity model responses. The supplemental additive output SM term $q^{(i)}$ is only applied locally, as in (27), to further improve the surrogate model accuracy in the vicinity of the current design.
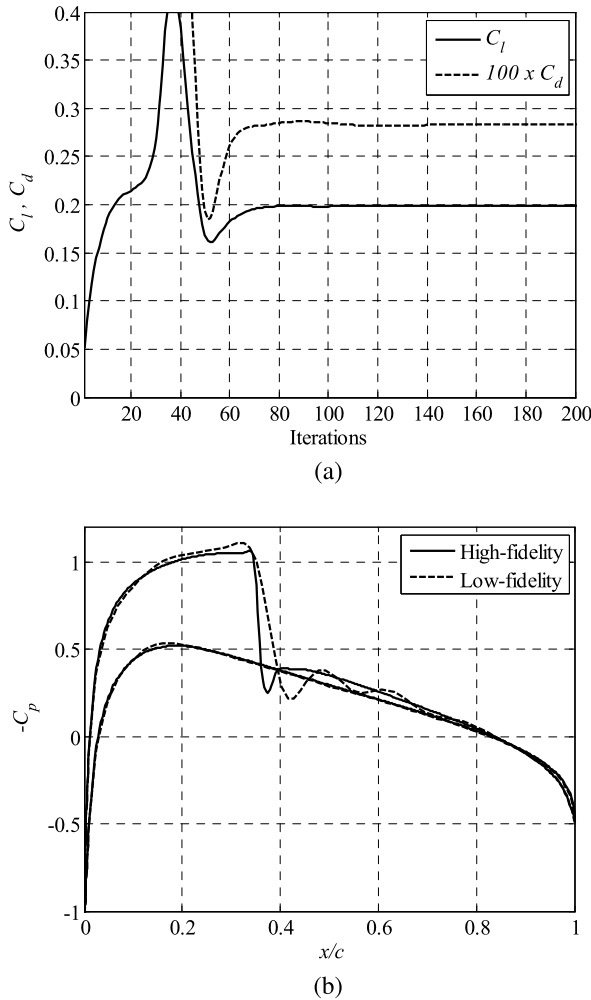
Fig. 6 Simulation results for NACA 0012 at Mach number $M_\infty = 0.75$ and angle of attack $\alpha = 1$ deg: (**a**) evolution of the lift and drag coefficients obtained by the low-fidelity model, (**b**) comparison of the pressure distributions obtained by the high- and low-fidelity models

4.4 Case Description

Four design cases are presented: three lift maximizations (Cases 1–3) and one drag minimization (Case 4). For Cases 1 through 3, the objective is to maximize the lift coefficient $C_{l.f}$, subject to constraints on drag ($C_{d.f} \leq C_{d.\max}$) and nondi- mensionalized airfoil cross-sectional area with the chord squared ($A \geq A_{\min}$). For Case 4, the objective is to minimize the drag, subject to constraints on lift coefficient ($C_{l.f} \geq C_{l.\min}$) and nondimensionalized airfoil cross-sectional area with the chord squared ($A \geq A_{\min}$).
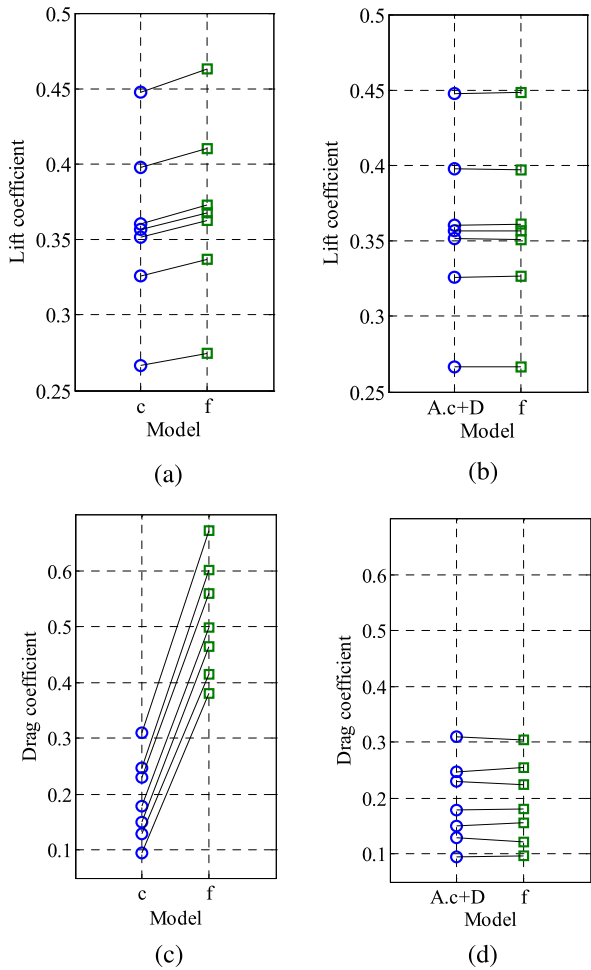
Fig. 7 The effect of output SM (26) on the low- and high-fidelity model alignment: (**a**) high- (○) and low-fidelity (□) lift coefficient for selected airfoil geometries, (**b**) high- (○) and output-S-M-aligned low-fidelity (□) lift coefficient for corresponding geometries, (**c**) the same as (**a**) but for the drag coefficient, (**d**) the same as (**b**) but for the drag coefficient. The model misalignment is greatly reduced by applying both multiplicative and additive output SM. The alignment is further improved by the supplemental local additive output SM term $q^{(i)}$ (cf. (27))

For simplicity, and because we have a small number of design variables, the NACA four-digit method is used to parameterize the airfoil shapes. Although these airfoils are intended for subsonic flow, it is used here for demonstration purposes only, as the method has only three design parameters. The particulars of the method are given in the Appendix.

The NACA four-digit airfoil design variables are m (the maximum ordinate of the mean camber line as a fraction of the chord), p (the chordwise position of

the maximum ordinate), and t/c (the thickness-to-chord ratio). The design vector can be written as $\mathbf{x} = [m \; p \; t/c]^T$. The side constraints on the design variables are $0 \leq m \leq 0.1$, $0.2 \leq p \leq 0.8$, and $0.05 \leq t/c \leq 0.2$. Details of the test cases and optimization results are given in Table 2. The results are compared with the direct design optimization of the high-fidelity model using the pattern search algorithm. For the surrogate model optimization in the SM algorithm, the pattern search algorithm is also used. The termination condition for the SM algorithm is $\|\mathbf{x}^{(i)} - \mathbf{x}^{(i-1)}\| < 10^{-3}$.

4.5 Results

Consider Case 1 in Table 2, where the initial airfoil design is NACA 2412 and the drag constraint is violated. The direct method and the SM algorithm obtain comparable optimized designs by reducing camber, placing the location of the maximum camber relatively aft, and reducing the thickness. The SM algorithm required 210 surrogate model evaluations (N_c) and 4 high-fidelity model evaluations (N_f), yielding an equivalent number of high-fidelity model evaluations of less than 7. The direct method required 96 high-fidelity model evaluations.

In Case 2, the initial design is NACA 2412, which is feasible for the assumed constraints. The SM algorithm is able to obtain a better optimized design than the direct method. The shape changes are similar to those of Case 1, except that the camber is increased. The effects on the pressure distribution can be observed in Fig. 8: the shock strength is reduced by reducing the thickness, and the aft camber location opens up the pressure distribution behind the shock to increase the lift. The SM algorithm required less than 9 equivalent high-fidelity model evaluations (260 surrogate and 5 high-fidelity).

The optimization history for Case 2 is shown in Fig. 9. In particular, one can observe a convergence plot, as well as the evolution of the objective function, the lift coefficient, and the drag coefficient. It follows that the SM algorithm exhibits a good convergence pattern and enforces the drag limitation to be satisfied while increasing the lift coefficient as much as possible.

Case 3 has an initial design with higher camber and thinner section than the other cases, namely the NACA 3210. The SM algorithm achieves a better design than the direct method. Now the camber is reduced, but the location of the maximum camber is again moved aft and the thickness is slightly reduced. Less than 9 equivalent high-fidelity model evaluations are required.

In Case 4, the drag minimization case, the initial design is NACA 2412 and the lift constraint is slightly violated. Similar optimized designs are obtained by the direct method and the SM algorithm. The camber is reduced, the maximum camber moved aft, and the thickness reduced. As a result, the shock is weakened, and the lift improved by opening the pressure distribution behind the shock (see Fig. 10). The SM algorithm required 5 equivalent high-fidelity model evaluations (160 surrogate and 3 high-fidelity), whereas the direct method required 110.

Overall, it can be observed that the SM performance is consistent across the considered test cases. The average airfoil design cost is equivalent to about 5 to 9

Table 2 Numerical results for four test cases. Shown are results for the initial design, direct optimization, and optimization using space mapping

Variable	Case 1 (Lift maximization) $M_\infty = 0.75$, $\alpha = 0°$, $C_{d,\max} = 0.005$, $A_{\min} = 0.075$			Case 2 (Lift maximization) $M_\infty = 0.70$, $\alpha = 1°$, $C_{d,\max} = 0.006$, $A_{\min} = 0.075$		
	Initial	Direct	SM	Initial	Direct	SM
m	0.02	0.0140	0.0150	0.02	0.0200	0.0237
p	0.40	0.7704	0.7463	0.40	0.7467	0.6531
t/c	0.12	0.1150	0.1140	0.12	0.1200	0.1148
C_l	0.4745	0.5572	0.5650	0.5963	0.8499	0.8909
C_{dw}	0.0115	0.0050	0.0050	0.0047	0.0060	0.0060
A	0.0808	0.0774	0.0767	0.0808	0.0808	0.0773
N_c	–	0	210	–	0	260
N_f	–	96	4	–	59	5
Cost	–	96	<7	–	59	<9

Variable	Case 3 (Lift maximization) $M_\infty = 0.75$, $\alpha = 1°$, $C_{d,\max} = 0.0041$, $A_{\min} = 0.065$			Case 4 (Drag minimization) $M_\infty = 0.70$, $\alpha = 1°$, $C_{l,\min} = 0.6$, $A_{\min} = 0.075$		
	Initial	Direct	SM	Initial	Direct	SM
m	0.03	0.0080	0.0100	0.02	0.0180	0.0180
p	0.20	0.6859	0.6929	0.40	0.5207	0.5290
t/c	0.10	0.1044	0.0980	0.12	0.1141	0.1113
C_l	0.8035	0.4641	0.5281	0.5963	0.6001	0.6002
C_{dw}	0.0410	0.0041	0.0041	0.0047	0.0019	0.0017
A	0.0675	0.0703	0.0659	0.0808	0.0768	0.0749
N_c	–	0	260	–	0	160
N_f	–	121	5	–	110	3
Cost	–	121	<9	–	110	5

high-fidelity model evaluations, which corresponds to a cost savings of 80 percent or more depending on a test case, when compared to direct airfoil optimization using pattern search.

5 Wing Design

In this section, the SM algorithm is demonstrated for the design of a three-dimensional wing shape. Again, transonic flow is considered, but a steady viscous Reynolds-averaged Navier–Stokes (RANS) CFD model is used with an unstruc-
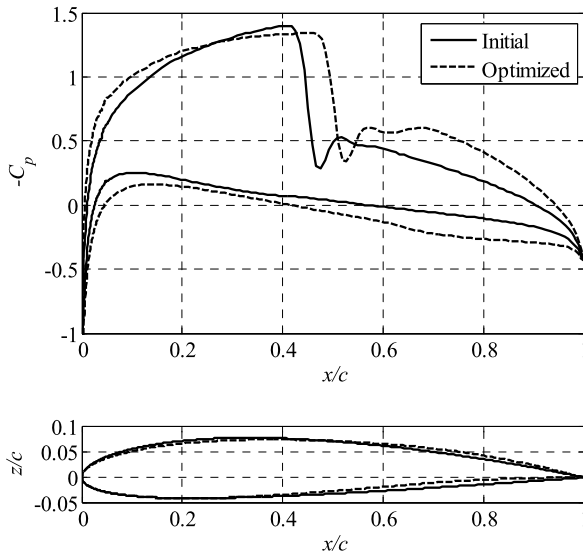
Fig. 8 Initial and optimized pressure distributions and airfoil shapes for Case 2

tured grid. Still, the variable-resolution approach is employed. One design case is considered, but optimization runs for two different initial designs are presented.

5.1 High-Fidelity Model

The flow is steady, compressible, viscous, and without body forces, mass diffusion, chemical reactions, or external heat addition. The RANS equations with the one-equation Spalart-Allmaras turbulence model [32] are solved. Air is modeled by the ideal gas law and the Sutherland dynamic viscosity model.

The far field is configured in a box topology where the wing root airfoil is placed in the center of the symmetry plane, with its leading edge placed at the origin. The far field extends 100 chord lengths in all directions upstream, above, below, and aft of the wing. The computational domain, along with the boundary conditions, is shown in Fig. 11.

An unstructured tri/tetra shell grid is created on all surfaces. The shell grid from the wing is then extruded into the volume where the volume is flooded with tri/tetra elements. The grid is made dense close to the wing, where it then gradually grows in size as it moves away from the wing surfaces. To capture the viscous boundary layer an inflation layer or a prism layer is created on the wing surfaces as well. The grid is generated using ANSYS ICEM CFD and is shown in Fig. 12.

In the stream-wise direction, the number of elements on the wing is set to 100 on both the upper and lower surfaces. The bigeometric bunching law with a growth ratio of 1.2 is employed in the stream-wise direction over the wing to obtain a more dense
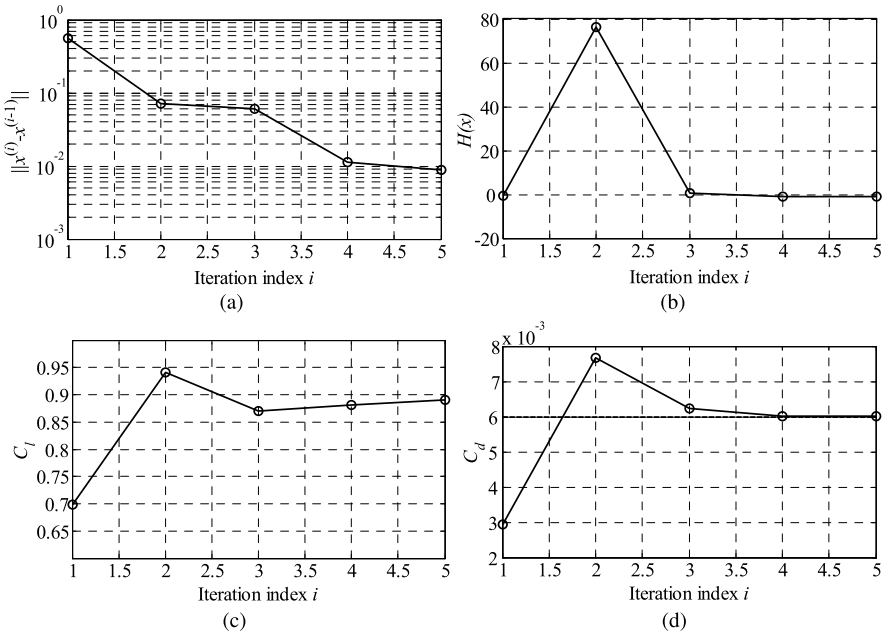
Fig. 9 Optimization history for Case 2: (**a**) convergence plot, (**b**) evolution of the objective function, (**c**) evolution of the lift coefficient, and (**d**) evolution of the drag coefficient (drag constraint marked using a *dashed horizontal line*). The graphs show all high-fidelity function evaluations performed in the optimization
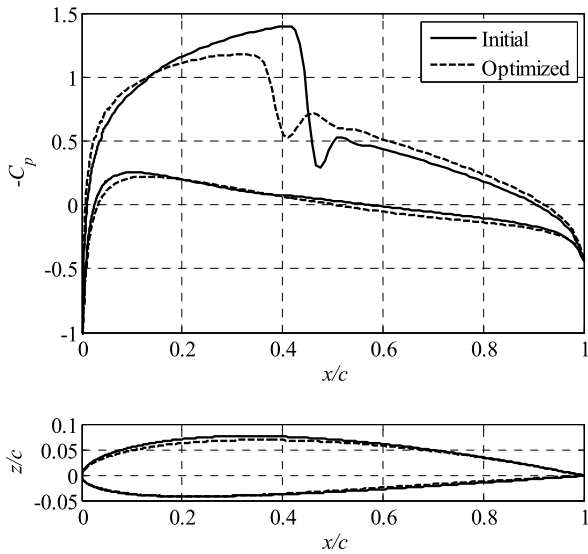

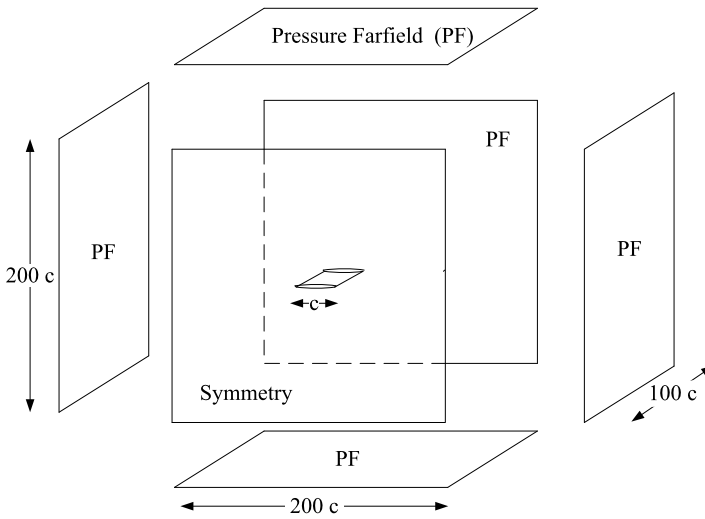**Fig. 10** Initial and optimized pressure distributions and airfoil shapes for Case 4

Fig. 11 Far field configured as a box topology. The leading edge of the wing root airfoil is placed at $(x, y, z) = (0, 0, 0)$

element distribution at the leading edge and the trailing edge. This is done in order to capture the high pressure gradient at the leading edge and potential separation at the trailing edge. The minimum element size of the wing in the stream-wise direction is set to 0.1 %c, and it is located at the leading and trailing edge. In the span-wise direction, elements are distributed uniformly and the number of elements is set to 100 over the semi-span. A prism layer is used to capture the viscous boundary layer. This layer consists of a number of structured elements that grow in size normal to the wing surface into the domain volume. The inflation layer has an initial height of $5 \times 10^{-6}c$ where it is grown 20 layers into the volume using an exponential growth law with a ratio of 1.2. The initial layer height is chosen so that $y^+ < 1$ at all nodes on the wing.

The numerical fluid flow simulations are performed using the computer code ANSYS FLUENT [34]. The implicit density-based solver is applied using the Roe flux-difference splitting (FDS) flux type. The spatial discretization schemes are set to second order for all variables, and the gradient information is found using the Green–Gauss node-based method. The residuals, which are the sum of the L^2 norms of all governing equations in each cell, are monitored and checked for convergence. For the high-fidelity model, a solution is considered to be converged if the residuals have dropped by six orders of magnitude, or the total number of iterations has reached 1,000. Also, the lift and drag coefficients are monitored for convergence.

A grid convergence study is conducted using the ONERA M6 wing [35]. The flow past the ONERA M6 wing is simulated at various grid resolutions at $Re_{\infty,c_{\mathrm{mac}}} = 11.72 \times 10^6$, $M_\infty = 0.8395$, and angle of attack $\alpha = 3.06°$, where c_{mac} is the mean aerodynamic chord length. The flow conditions are selected to match the
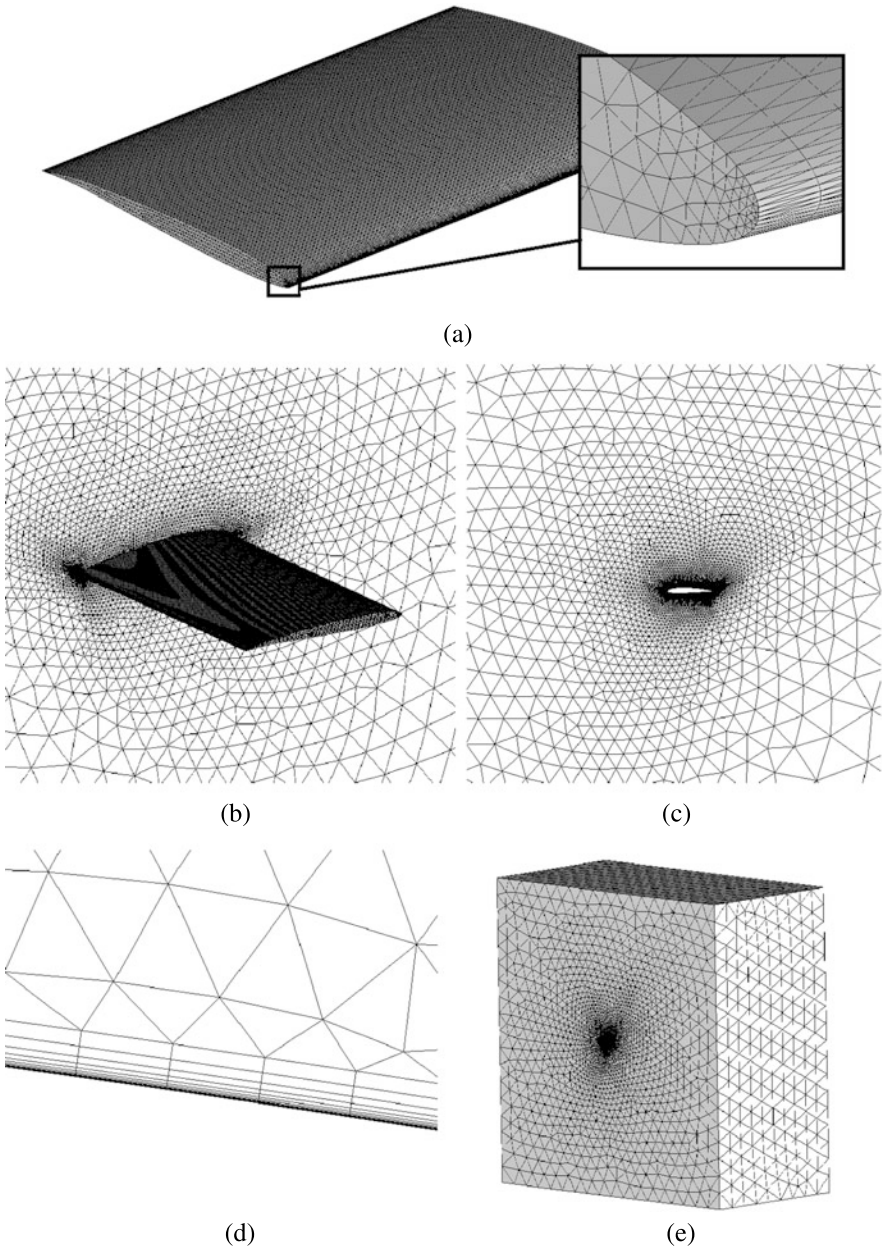
(a)

(b)

(c)

(d)

(e)

Fig. 12 Shell grid shown for all surfaces: (**a**) wing shell grid, (**b**)–(**c**) symmetry plane where the wing is placed, (**d**) prism layer applied close to the wing surface to capture the viscous boundary layer, (**e**) far-field volume
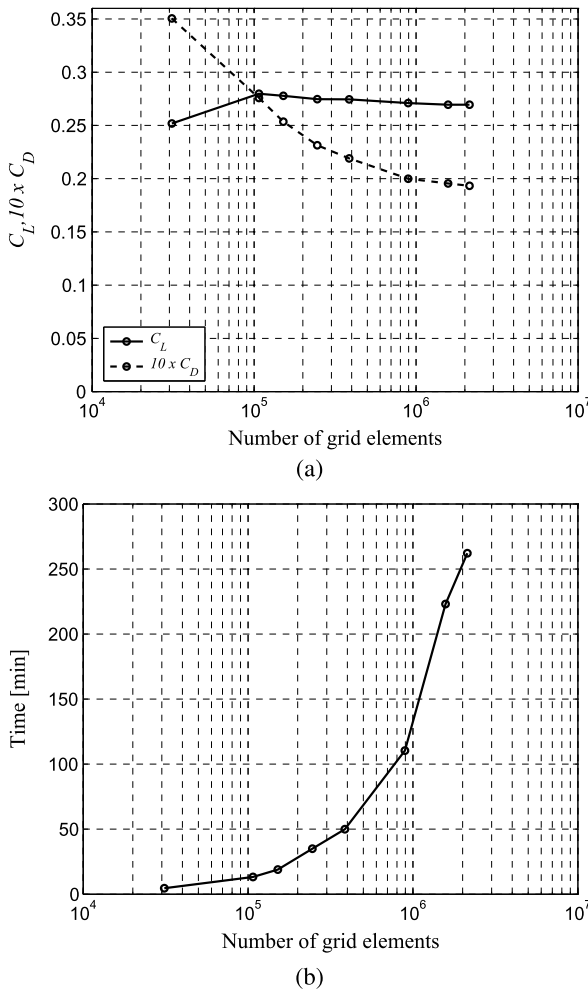
(a)

(b)

Fig. 13 Grid convergence study using the ONERA M6 wing at $M_\infty = 0.8395$ and angle of attack $\alpha = 3.06°$: (**a**) lift (C_L) and drag (C_D) coefficients versus number of grid elements, (**b**) simulation time versus number of grid elements

experimental flow conditions of an ONERA M6 wing experiment 2308 conducted by Schmitt and Charpin [36].

The grid convergence study, shown in Fig. 13a, revealed that 1,576,413 cells are needed for convergence in lift. The drag, however, can still be improved, as is evident from Fig. 13a, where convergence has not been reached due to limitations in the computational resources. However, we proceed with this grid as the high-fidelity model grid. The overall simulation time needed for one high-fidelity CFD simulation was around 223 min, as shown in Fig. 13b, executed on four Intel-i7-
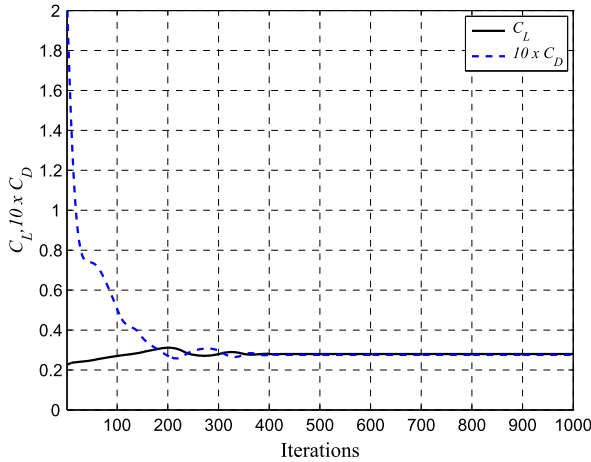
Fig. 14 Lift and drag coefficient convergence plot for low-fidelity model obtained in grid convergence study simulation using ONERA M6 wing at Mach number $M_{\infty} = 0.8395$ and angle of attack $\alpha = 3.06°$

2600 processors in parallel. This execution time is based on 1,000 solver iterations, where the solver terminated due to the maximum number of iterations limit.

5.2 Low-Fidelity Model

The low-fidelity model $c(\mathbf{x})$ is constructed in the same way as the high-fidelity model $f(\mathbf{x})$, but with a coarser grid discretization and with a relaxed convergence criterion. Referring back to the grid study of the previous section, and inspecting Fig. 13a, we make our selection for the coarse low-fidelity model. Based on time and accuracy with respect to lift and drag, we select the grid parameters that represent the second point from the left with 107,054 elements. The time taken to evaluate the low-fidelity model is 13.2 min on four Intel-i7-2600 processors in parallel.

Inspecting further the lift and drag convergence plot for the low-fidelity model in Fig. 14, we note that the solution has converged after about 500 iterations. The maximum number of iterations for the low-fidelity model is therefore set to 500 iterations. This reduces the overall simulation time to 6.6 min. The ratio of the simulation times of the high- and low-fidelity models in this case is high/low $= 223/6.6 \approx 34$. This is based on the solver using all 500 iterations in the low-fidelity model to obtain a solution.
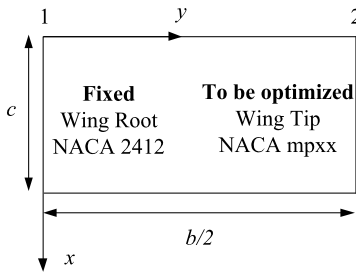
Fig. 15 A planform view of a constant chord rectangular wing constructed by two NACA airfoils. Each airfoil has its own set of design parameters

5.3 Surrogate Model

The low-fidelity CFD model c turns out to be very noisy. In order to alleviate the problem, a second-order polynomial approximation model [7] is constructed using $n_c = 50$ training points sampled using Latin hypercube sampling (LHS) [6] using the low-fidelity CFD model. The polynomial approximation model is defined as

$$\overline{c}(\mathbf{x}) = c_0 + \mathbf{c}_1^T \mathbf{x} + \mathbf{x}^T \mathbf{c}_2 \mathbf{x}, \tag{36}$$

where $\mathbf{c}_1 = [c_{1.1} \ c_{1.2} \ c_{1.3}]^T$ and $\mathbf{c}_2 = [c_{2.ij}]_{i,j=1,2,3}$. The coefficients c_0, $\mathbf{c}_1$, $\mathbf{c}_2$ are found by solving the linear regression problem

$$\overline{c}(\mathbf{x}^k) = c(\mathbf{x}^k), \tag{37}$$

where $k = 1, \ldots, n_c$. The resulting second-order polynomial model $\overline{c}$ has nice analytical properties, such as smoothness and convexity. The surrogate model is then constructed as described in Sect. 3.

5.4 Case Description

For demonstration purposes, an unswept and untwisted wing is considered. The wing is constructed by two NACA four-digit airfoils, located at the root and tip, as shown in Fig. 15. The root is fixed to the NACA 2412 airfoil and the tip airfoil is to be designed. The initial design $\mathbf{x}^{(0)}$ for the wing tip is chosen at random at the start of each optimization run. The normalized semi-wingspan is set as twice the wing chord length c as $(b/2) = 2c$. All other wing parameters are kept fixed. The design vector can be written as $\mathbf{x} = [m \ p \ t/c]^T$, where the variables represent the wing tip NACA four-digit airfoil parameters (see the Appendix).

The objective is to maximize the lift coefficient $C_{L.f}$, subject to constraints on the drag coefficient $C_{D.f} \leq C_{D.\max} = 0.03$ and the wing tip normalized cross-sectional area $A \geq A_{\min} = 0.01$. The side constraints on the design variables are $0.02 \leq m \leq 0.03$, $0.7 \leq p \leq 0.9$ and $0.06 \leq t/c \leq 0.08$.

Table 3 Numerical comparison of Run 1 and Run 2, initial and optimized designs. The ratio of the high-fidelity model evaluation time to the low-fidelity time is 34

Variable	Initial		Optimized	
	Run 1	Run 2	Run 1	Run 2
m	0.0200	0.0259	0.0200	0.0232
p	0.7000	0.8531	0.8725	0.8550
t/c	0.0628	0.0750	0.0793	0.0600
C_L	0.2759	0.3426	0.3047	0.3388
C_D	0.0241	0.0344	0.0311	0.0307
C_L/C_D	11.4481	9.9593	9.7974	11.0358
A	0.0422	0.0505	0.0534	0.0404
N_c	–	–	50	50
N_f	–	–	8	7
Total cost	–	–	<10	<9

5.5 Results

Two optimization runs were performed, denoted as Run 1 and Run 2. The numerical results are given in Table 3, and the initial and optimized airfoil cross sections are shown in Fig. 16a and Fig. 16b, respectively.
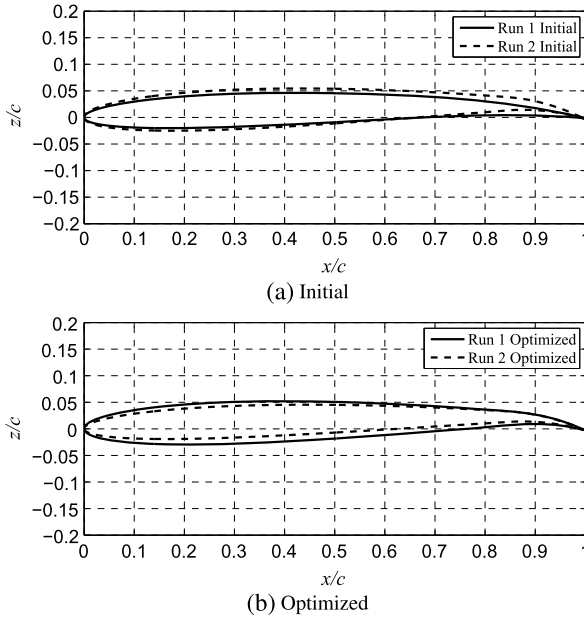

(a) Initial

(b) Optimized

Fig. 16 A comparison of Run 1 and Run 2: (**a**) initial and (**b**) optimized designs. Run 1 is shown with a *solid lines* (–), and Run 2 with *dashed lines* (- -)
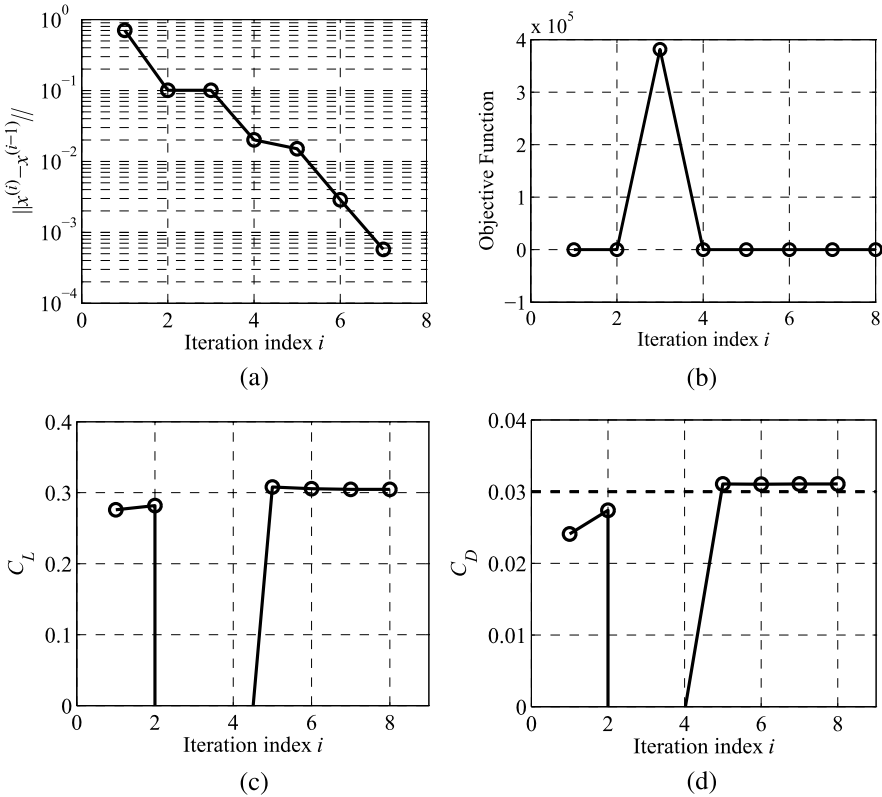
Fig. 17 Optimization history for Run 1: (**a**) convergence history, (**b**) evolution of the objective function, (**c**) evolution of lift coefficient, and (**d**) evolution of drag coefficient where *dashed line* (- -) is the drag constraint

In Run 1, the lift is increased by $+10$ % and the drag is pushed above its constraint at $C_{D,\max} = 0.03$, where the optimized drag coefficient is $C_D = 0.0311$. The drag constraint is violated slightly, or by $+4$ %, which is within the 5 % constraint tolerance band. The lift-to-drag ratio is decreased by -14 %. The SM algorithm requires less than 10 high-fidelity model evaluations, where 50 low-fidelity model evaluations (N_c) are used to create the approximation model and 8 high-fidelity model evaluations (N_f) are used for each design iteration. It is evident that the optimized wing tip airfoil is thicker as the normalized cross-sectional area is increased by $+26$ %, and the increased drag can be related to the increment in area. No change occurs in the camber m, but the location of the maximum camber p has moved slightly aft. The convergence history is shown in Fig. 17.

The initial design for Run 2 violates the drag constraint. The SM algorithm is, however, able to push the drag to its constraint limit, where the optimized drag coefficient is slightly violated, by $+2$ %. While the drag is decreased by -11 %, the lift is maintained and only drops by -1 %. As a result, the lift-to-drag ratio is increased
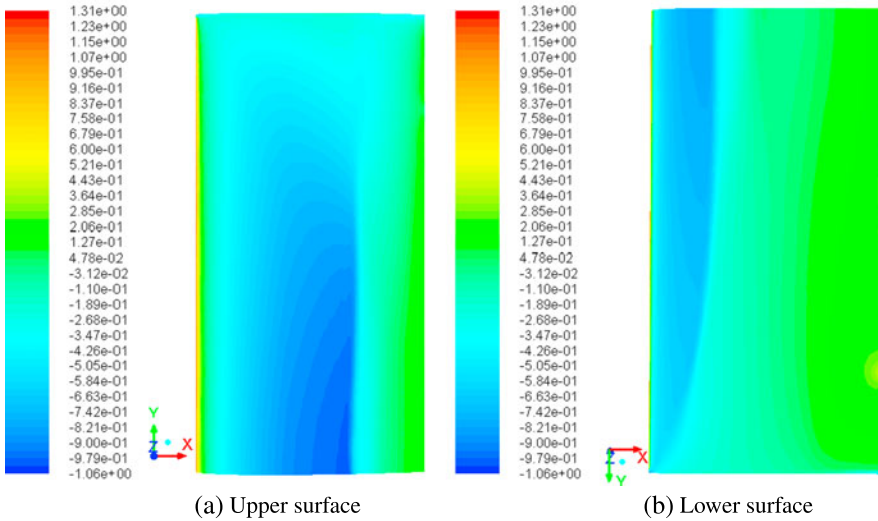
(a) Upper surface   (b) Lower surface

Fig. 18 Run 1 planform pressure coefficient contour plots of the initial design geometry. (**a**) The *upper surface* shows shocks at midsection of the wing; (**b**) the *lower surface* shows one shock at the leading edge

by +11 %. The SM algorithm requires less than 9 high-fidelity model evaluations (50 low-fidelity model evaluations used to create the approximation model and 7 high-fidelity model evaluations). The optimized wing tip airfoil is thinner than the initial design (the normalized cross-sectional area is reduced by −20 %). Small changes are made to the camber m and the maximum camber location p.

Comparing Runs 1 and 2, we note that, although they start from different initial designs, the optimized designs show similarities in two of three design variables, namely, the maximum camber m and maximum camber location p. The third, the airfoil thickness t/c, differs by approximately 2 %. The shock on the mid-wing has been moved aft, on both the upper and the lower surfaces (see Figs. 18, 19, 20, 21). Also, note that a second shock was formed near the tip on the upper surface. This causes the drag and the lift to increase.

6 Conclusions

A robust and computationally efficient optimization methodology for the design of aerodynamic surfaces is presented. The approach exploits a low-fidelity model that is corrected using the space mapping technique to create a fast and reliable prediction tool (the surrogate) that is subsequently used to yield an approximate optimum design of the expensive, high-fidelity model at low CPU cost. A space mapping correction is applied both to the objectives and constraints in a two-stage process with a quasi-global space mapping alignment supplemented by a local one that ensures
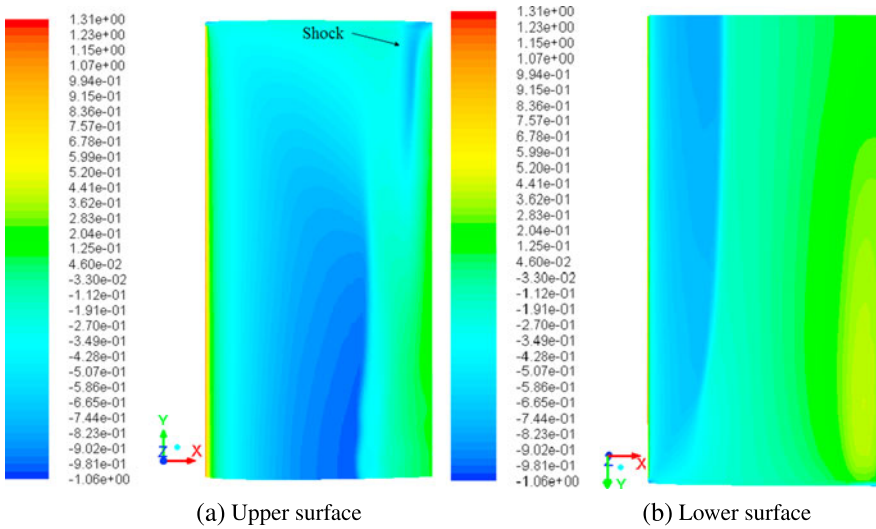
(a) Upper surface   (b) Lower surface

Fig. 19 Run 1 planform pressure coefficient contour plots of the optimized design geometry. (**a**) The *upper surface* shows two shocks, one at midsection of the wing and one close to the wing tip at the trailing edge. (**b**) The *lower surface* shows one shock at the leading edge

perfect alignment between the surrogate and the high-fidelity model. Applications for transonic airfoil and wing design are demonstrated with the optimized designs obtained at a computational cost corresponding to a few high-fidelity model evaluations.

Appendix

The NACA four-digit airfoils are denoted by convention as NACA *mpxx*, where *m* is the maximum ordinate of the mean camber line as a percentage of the chord, *p* is the chordwise position in tens of percentages of the maximum ordinate, and *xx* is the thickness-to-chord ratio in percentages of the chord (t/c). The NACA airfoils are constructed by combining a thickness function $z_t(x)$ with a mean camber line function $z_c(x)$ [25]. The x and z coordinates are

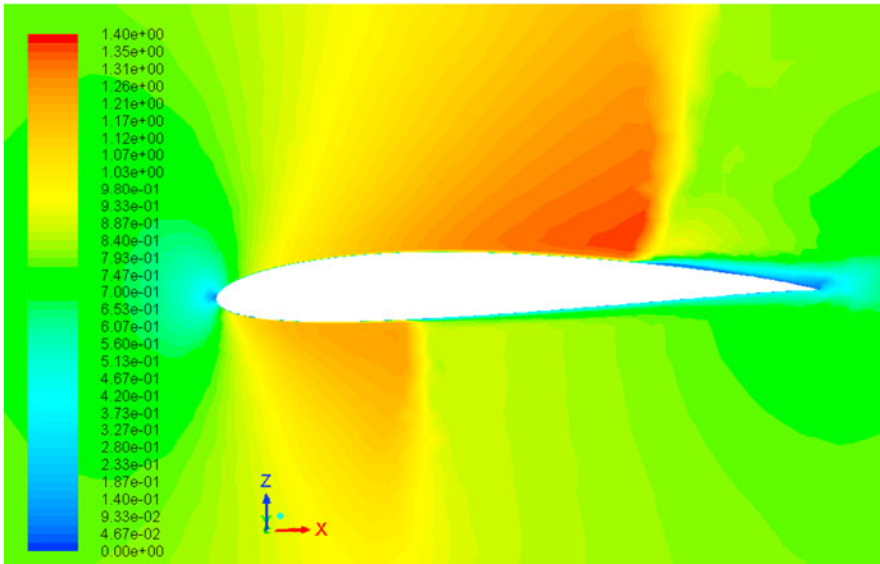$$x_{u,l} = x \mp z_t \sin\theta, \tag{38}$$

$$z_{u,l} = z_c \pm z_t \cos\theta, \tag{39}$$

where u and l are the upper and lower surfaces, respectively, and

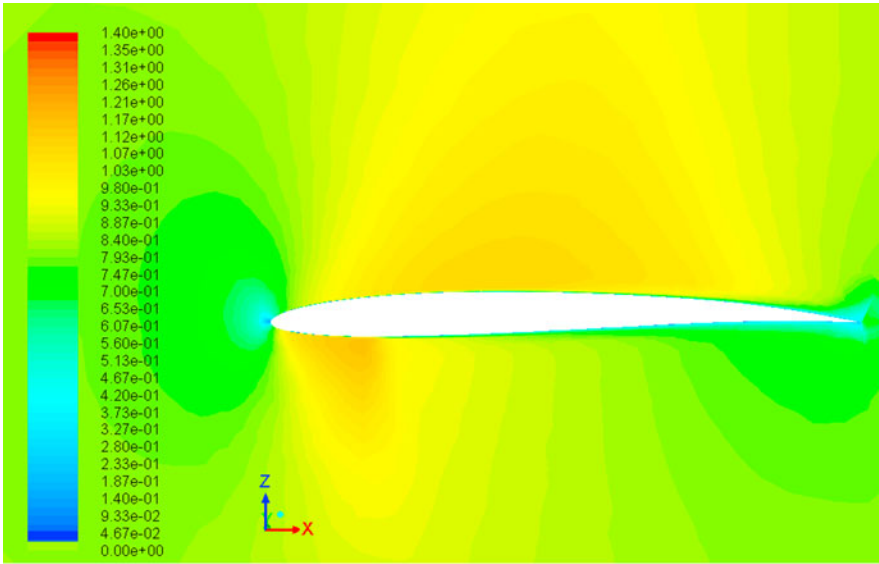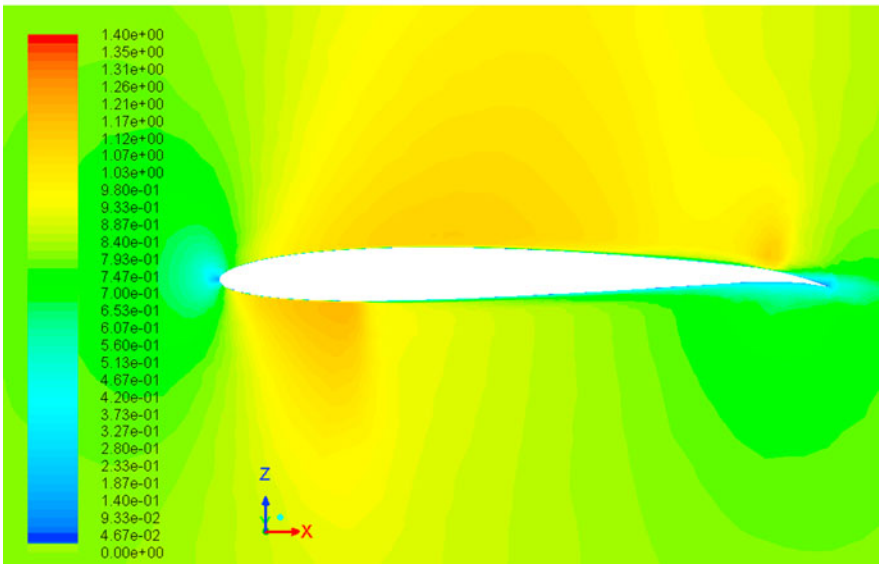$$\theta = \tan^{-1}\left(\frac{dz_c}{dx}\right), \tag{40}$$
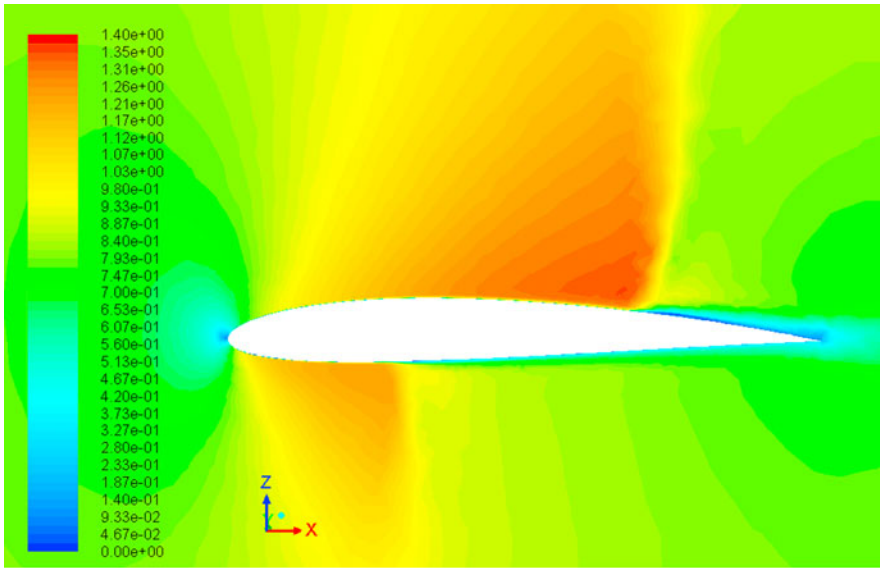
(a) Initial

(b) Optimized

Fig. 20 Run 1 Mach number contour plot at $y/(b/2) = 0.2$, where $M_\infty = 0.8395$ and angle of attack $\alpha = 0°$. (**a**) Initial design, (**b**) optimized design

(a) Initial

(b) Optimized

Fig. 21 Run 1 Mach number contour plot at $y/(b/2) = 0.8$, where $M_\infty = 0.8395$ and angle of attack $\alpha = 0°$: (**a**) initial design, (**b**) optimized design. Notice the shock at the trailing edge
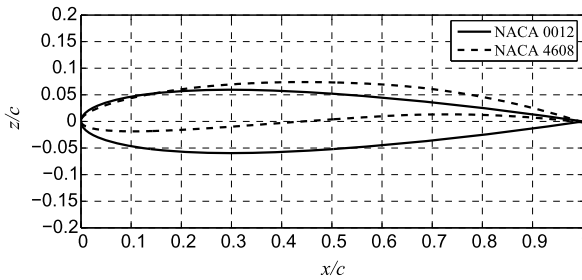
Fig. 22 Examples of two airfoil sections generated with the NACA four-digit method. NACA 0012 ($m = 0, p = 0, t/c = 0.12$) is shown by *solid line* (–); NACA 4608 ($m = 0.04, p = 0.6, t/c = 0.08$) is shown by a *dashed line* (- -)

is the mean camber line slope. The NACA four-digit thickness distribution is given by

$$z_t = t\left(a_0 x^{1/2} - a_1 x a_2 x^2 + a_3 x^3 - a_4 x^4\right), \tag{41}$$

where $a_0 = 1.4845, a_1 = 0.6300, a_2 = 1.7580, a_3 = 1.4215, a_4 = 0.5075$, and t is the maximum thickness. The mean camber line is given by

$$z_c = \begin{cases} \frac{m}{p^2}(2px - x^2), & x < p, \\ \frac{m}{(1-p)^2}(1 - 2p + 2px - x^2), & x \geq p. \end{cases} \tag{42}$$

Examples of airfoils generated with the NACA four-digit method are shown in Fig. 22.

References

1. Jameson, A.: Aerodynamic design via control theory. J. Sci. Comput. **3**, 233–260 (1988)
2. Braembussche, R.A.: Numerical Optimization for Advanced Turbomachinery Design (2008)
3. Dumas, L.: CFD-Based Optimization for Automotive Aerodynamics (2008)
4. Percival, S., Hendrix, D., Noblesse, F.: Hydrodynamic optimization of ship hull forms. Appl. Ocean Res. **23**(6), 337–355 (2001)
5. Queipo, N.V., Haftka, R.T., Shyy, W., Goel, T., Vaidyanathan, R., Tucker, P.K.: Surrogate-based analysis and optimization. Prog. Aerosp. Sci. **41**(1), 1–28 (2005)
6. Forrester, A.I.J., Keane, A.J.: Recent advances in surrogate-based optimization. Prog. Aerosp. Sci. **45**(1–3), 50–79 (2009)
7. Koziel, S., Ciaurri, D.E., Leifsson, L.: Surrogate-based methods. In: Computational Optimization and Applications in Engineering and Industry, vol. 359. Springer, Berlin (2011)
8. Wild, S.M., Regis, R.G., Shoemaker, C.A.: Orbit: optimization by radial basis function interpolation in trust-regions. SIAM J. Sci. Comput. **30**(6), 3197–3219 (2008)
9. Simpson, T.W., Poplinski, J.D., Koch, P.N., Allen, J.K.: Metamodels for computer-based engineering design: survey and recommendations. Eng. Comput. **17**(2), 129–150 (2001)
10. Journel, A.G., Huijbregts, C.J.: Mining Geostatistics. Academic Press, London (1978)
11. O'Hagan, A., Kingman, J.F.C.: Curve fitting and optimal design for prediction. J. R. Stat. Soc. Ser. B Methodol., 1–42 (1978)

12. Haikin, S.: Neural Networks: A Comprehensive Foundation. Prentice-Hall, Englewood Cliffs (1998)
13. Minsky, M., Papert, S.: Perceptrons: An Introduction to Computational Geometry. MIT Press, Cambridge (1969)
14. Smola, A.J., Schölkopf, B.: A tutorial on support vector regression. Stat. Comput. **14**(3), 199–222 (2004)
15. Søndergaard, J.: Optimization using surrogate models by the space mapping technique. Ph.D. thesis, Technical University of Denmark, Informatics and mathematical modelling (2003)
16. Leifsson, L., Koziel, S.: Variable-fidelity aerodynamic shape optimization. In: Computational Optimization, Methods and Algorithms, vol. 356. Springer, Berlin (2011)
17. Bandler, J.W., Cheng, Q.S., Dakroury, S.A., Mohamed, A.S., Bakr, M.H., Madsen, K., Sondergaard, J.: Space mapping: the state of the art. IEEE Trans. Microw. Theory Tech. **52**(1), 337–361 (2004)
18. Alexandrov, N.M., Lewis, R.M.: An overview of first-order model management for engineering optimization. Optim. Eng. **2**(4), 413–430 (2001)
19. Koziel, S., Cheng, Q., Bandler, J.: Space mapping. IEEE Microw. Mag. **9**(6), 105–122 (2008)
20. Echeverria, D., Hemker, P.W.: Space mapping and defect correction. Comput. Methods Appl. Math. **5**(2), 107–136 (2005)
21. Koziel, S.: Shape-preserving response prediction for microwave design optimization. IEEE Trans. Microw. Theory Tech. **58**(11), 2829–2837 (2010)
22. Robinson, T.D., Willcox, K.E., Eldred, M.S., Haimes, R.: Multifidelity optimization for variable complexity design. In: Proceedings of the 11th AIAA/ISSMO Multidisciplinary Analysis and Optimization Conference, Portsmouth, VA (2006)
23. Koziel, S., Leifsson, L.: Knowledge-based airfoil shape optimization using space mapping. In: 30th AIAA Applied Aerodynamics Conference, New Orleans, Louisiana, June 25–28 (2012), AIAA 2012-3016
24. Jonsson, E., Koziel, S., Leifsson, L.: Transonic wing optimization by variable-resolution modeling and space mapping. In: 2nd Int. Conf. on Simulation and Modeling Methodologies, Technologies, and Applications (SIMULTECH), Rome, Italy, July 28–31 (2012)
25. Abbott, I.H., Von Doenhoff, A.E.: Theory of Wing Sections: Including a Summary of Airfoil Data. Dover Publications, New York (1959)
26. Hicks, R.M., Henne, P.A.: Wing design by numerical optimization. J. Aircr. **15**(7), 407–412 (1977)
27. Derksen, R.W., Rogalsky, T.: Bezier-PARSEC: an optimized aerofoil parameterization for design. Adv. Eng. Softw. **41**, 923–930 (2010)
28. Leoviriyakit, K., Kim, S., Jameson, A.: Viscous aerodynamic shape optimization of wings including planform variables. In: 21st AIAA Applied Aerodynamics Conference, Orlando FL (2003), AIAA Paper AIAA-2003-3791
29. Koziel, S., Cheng, Q.S., Bandler, J.W.: Implicit space mapping with adaptive selection of preassigned parameters. IET Microw. Antennas Propag. **4**(3), 361–373 (2010)
30. Koziel, S., Bandler, J.W., Madsen, K.: A space mapping framework for engineering optimization: theory and implementation. IEEE Trans. Microw. Theory Tech. **54**(10), 3721–3730 (2006)
31. Zhu, J., Bandler, J.W., Nikolova, N.K., Koziel, S.: Antenna optimization through space mapping. IEEE Trans. Antennas Propag. **55**(3), 651–658 (2007)
32. Tannehill, J.C., Anderson, D.A., Pletcher, R.H.: Computational Fluid Mechanics and Heat Transfer. Taylor & Francis Group, London (1997)
33. ANSYS: ANSYS ICEM CFD. Southpointe 275 Technology Drive, Canonburg, PA 15317, release 13.0 edition, November (2010)
34. ANSYS: ANSYS FLUENT Theory Guide. ANSYS, Southpointe 275 Technology Drive, Canonburg PA 15317, release 13.0 edition, November (2010).

35. NASA: ONERA M6 wing validation case (2008). http://www.grc.nasa.gov/WWW/wind/valid/m6wing/m6wing.html
36. Schmitt, V., Charpin, F.: Pressure distributions on the ONERA-M6-wing at transonic Mach numbers. Experimental Data Base for Computer Program Assessment. Report of the Fluid Dynamics Panel Working Group 04, AGARD AR 138, May (1979)